Int J Cardiovasc Imaging
DOI 10.1007/s10554-009-9508-4

ORIGINAL PAPER

Stent implant follow-up in intravascular optical coherence tomography images

Gozde Unal · Serhan Gurmeric · Stéphane Guy Carlier

Received: 20 February 2009 / Accepted: 30 August 2009

Abstract The objectives of this article are (i) to utilize computer methods in detection of stent struts imaged in vivo by optical coherence tomography (OCT) during percutaneous coronary interventions (PCI); (ii) to provide measurements for the assessment and monitoring of in-stent restenosis by OCT post PCI. Thirty-nine OCT cross-sections from seven pullbacks from seven patients presenting varying degrees of neointimal hyperplasia (NIH) are selected, and stent struts are detected. Stent and lumen boundaries are reconstructed and one experienced observer analyzed the strut detection, the lumen and stent area measurements, as well as the NIH thickness in comparison to manual tracing using the reviewing software provided by the OCT manufacturer (LightLab Imaging, MA, USA). Very good agreements were found between the computer methods and the expert evaluations for lumen cross-section area (mean difference = 0.11 ± 0.70 mm^2; $r^2 = 0.98$, $P < 0.0001$) and the stent cross-section area (mean difference = 0.10 ± 1.28 mm^2; $r^2 = 0.85$, P value < 0.0001). The average number of detected struts was 10.4 ± 2.9 per cross-section when the expert identified 10.5 ± 2.8 ($r^2 = 0.78$, P value < 0.0001). For the given patient dataset: lumen cross-sectional area was on the average (6.05 ± 1.87 mm^2), stent cross-sectional area was (6.26 ± 1.63 mm^2), maximum angle between struts was on the average ($85.96 \pm 54.23°$), maximum, average, and minimum distance between the stent and the lumen were (0.18 ± 0.13 mm), (0.08 ± 0.06 mm), and (0.01 ± 0.02 mm), respectively, and stent eccentricity was (0.80 ± 0.08). Low variability between the expert and automatic method was observed in the computations of the most important parameters assessing the degree of neointimal tissue growth in stents imaged by OCT pullbacks. After further extensive validation, the presented methods might offer a robust automated tool that will improve the evaluation and follow-up monitoring of in-stent restenosis in patients.

Keywords OCT · Optical coherence tomography · Stent implant follow-up · In-stent restenosis assessment · Automatic strut detection

Abbreviations

OCT	Optical coherence tomography
ROI	Region of interest
NIH	NeoIntimal hyperplasia

G. Unal (✉) · S. Gurmeric
Faculty of Engineering and Natural Sciences,
Sabanci University, Istanbul, Turkey
e-mail: gozdeunal@sabanciuniv.edu

S. Gurmeric
e-mail: serhang@su.sabanciuniv.edu

S. G. Carlier
St Maria hospital, Halle and UZ, Brussels, Belgium
e-mail: sgcarlier@hotmail.com

Published online: 24 September 2009

Introduction

Optical Coherence Tomography (OCT) is a recent modality, which measures the intensity of back-reflected infrared light instead of acoustical waves using an interferometer since the speed of light is much faster than that of sound [1]. OCT was found useful as an intravascular imaging technique, and compared to IVUS in several works [2, 3]. The biggest advantage of OCT is its high resolution, on the order of 15 microns spatially, but at the cost of a decreased penetration depth of 0.5–2 mm. Both in vitro and in vivo studies [2, 4] have shown that the resolution of OCT can not only differentiate between typical constituents of atherosclerotic plaques, such as lipid, calcium, and fibrous tissue, but can also resolve the thin fibrous cap that is thought to be responsible for plaque vulnerability [5]. "OCT is superior to intravascular ultrasound for the detection and characterization of coronary atherosclerotic plaque composition, specifically for the differentiation of noncalcified, lipid-rich, or fibrous plaque." as reported by Rieber et al. [6].

Recent new developments in fast optical frequency domain imaging described a polarization sensitive OCT (PS-OCT) which is complementary to reflectance based OCT approaches [7]. PS-OCT allows simultaneous acquisition of both intensity and phase retardation images, which helps differentiation of lipid-rich plaques, thick fibrous plaques and calcifications as reported by [7]. Moreover, the much higher frame rate acquisition (>120/s) provided by optical frequency domain imaging (OFDI) will be very useful clinically, offering much faster pullback speed and alleviating the need of long balloon occlusion. Indeed, with a pullback speed of the imaging probe at 10–15 mm/s, a long coronary segment can be imaged while just flushing the artery with contrast similarly to a conventional angiogram acquisition.

Although Drug Eluting Stents (DES) suppress NIH strongly, in-stent restenosis after DES implantation still occurs [8]. Studies have shown that nonuniform circumferential stent strut distribution affects local drug concentration [9]. Number and distribution of the stent struts might also affect the magnitude of NIH after stent implantation in human coronary arteries [10]. Therefore, tracking of stent position, malapposition and neo-intimal tissue growth after stent implantation is clinically important.

Besides studies of stents by IVUS, a first study of SES follow-up using intra-coronary OCT pullbacks was performed in [11]. With OCT visualization, it was reported that most of the SES struts were covered with thin neointima but few of the SES showed full coverage. The study concluded that extended long-term follow-up with OCT may be helpful for SES coverage monitoring. More recent studies such as [12] have stressed the issue of late drug eluting stent thrombosis associated with late strut malapposition and positive vessel remodeling. A computerized system that would facilitate the assessment and quantification of stent malapposition, stent strut distribution and coverage appears clinically important.

To our knowledge, our study is the first automatic strut distribution analysis using OCT imaging to assist in the assessment of the degree of restenosis. The objective of this study was two-fold: (1) to explore the usability and performance of automatic computer methods to help with stent strut analysis in varying degrees of NIH scenarios; (2) to compare the computer analysis with expert analysis to correlate the results in OCT images.

The automated computer method and analysis we developed are compared to manual tracing using the reviewing software provided by the OCT manufacturer (LightLab Imaging MA, USA), called as LL software throughout the paper.

Methods

In this section, we describe the method that we have developed to detect struts in OCT pullback frames and the filtering process which helps in segmentation and analyzing stages. Generally, OCT images contain noise related to imaging process and artifacts such as reflections from bubble and sew-up stitch.[1] Therefore, first we preprocess the images to reduce or if possible remove noise and artifacts in order to increase the detection and measurement quality of the algorithm.

[1] Sew-up stitch artifact occurs due to a possible slight advance of the catheter before light beam scan of a cross-section image is completed. In the display image, it usually appears as a seaming artifact, which can not be removed but can be detected.

The main step of our algorithm entails segmentation of the lumen region on an OCT cross-section image and creation of a band in the arterial wall behind the lumen boundary. Analysis of the extracted Region of Interest (ROI) will facilitate stent strut detection. Particularly, strut shadows in this ROI are essential clues utilized in our algorithm.

Our approach consists of three different main operations: (1) preprocessing of the input OCT image and producing helper filtered images (Fig. 1); (2) initializing and propagating a spline inside the lumen region; (3) detection of struts, reconstruction of the stent boundary, and further analysis and measurements based on the computed lumen boundary, stent boundary and detected struts.

OCT imaging protocol: Automated pullback at 1 mm/s were conventionally performed using a M2 OCT Imaging Systems (LightLab Imaging, Inc., Westford, MA, USA) running at a frame rate of 15.6/s and a dedicated fibre-optic imaging wire (ImageWire LightLab Imaging Inc., Westford, MA, USA). Temporary blood clearance was obtained with a proximal occlusion balloon inflated to between 0.5–0.7 atm, while simultaneously flushing physiological saline through the distal lumen of the balloon catheter at a rate of 0.5 ml/s. Images have an axial resolution of about 15 microns. In vivo OCT pullbacks were recorded as rectangular data with image size of 200×752 pixels. These rectangular images are processed by our method and displayed after scan-conversion in a standard viewing format.

Study population: Seven pullbacks performed in previously stented coronary segments of seven patients presenting varying degrees of NIH were the test cases of our automated methods.

OCT pullback image analysis

Preprocessing

We show the results of preprocessing steps in Fig. 1: (a)"Original OCT display image"; (b) "Threshold filtered image" is the output of histogram based filtering operations; (c) "Row smoothed image" is utilized for the energy calculations over each line of the image that corresponds to light ray direction; (d) "Denoised image" is used in the segmentation process.

It can be observed in a typical OCT image that brighter pixel groups represent vessel wall, plaque, and stent struts. To enhance the desired information in the image, a histogram based filtering is applied first on the input OCT image. This filter helps to compensate brightness differences among frames. Figure 2 shows a typical histogram of an OCT image where the average pixel intensity values form a hill to the left of the intensity range. Next, darker pixels are removed from the output image according to an adaptive threshold value calculated from the histogram, to obtain the"threshold filtered image". At the second step, the "row smoothed image"is obtained as a result of a nonlinear filtering based on a one dimensional median filter to enhance the regions that hold struts and their shadows around the lumen region. To further eliminate the noise, the image is smoothed, and as can be observed in Fig. 1, the overall preprocessing produces a denoised and enhanced output that retains the desired features in the OCT image.

Lumen segmentation

A suitable contour representation to segment the lumen region of the OCT cross-section images is a

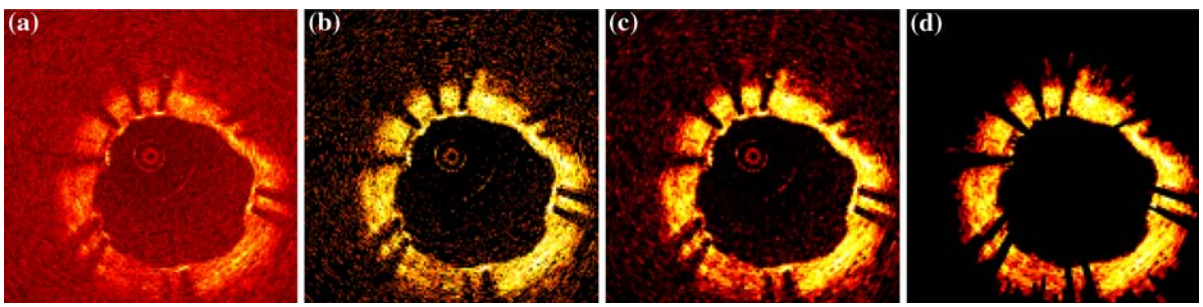

Fig. 1 OCT display image and filter results: **a** original image, **b** threshold filtered image, **c** row smoothed image, **d** denoised image

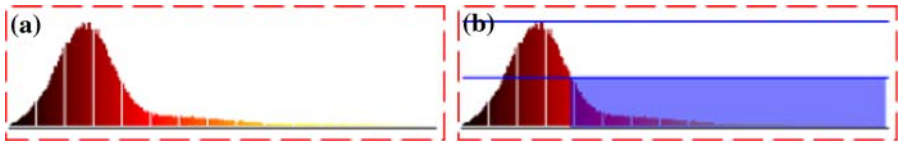

Fig. 2 **a** Typical scaled OCT image histogram, **b** threshold point and target density area

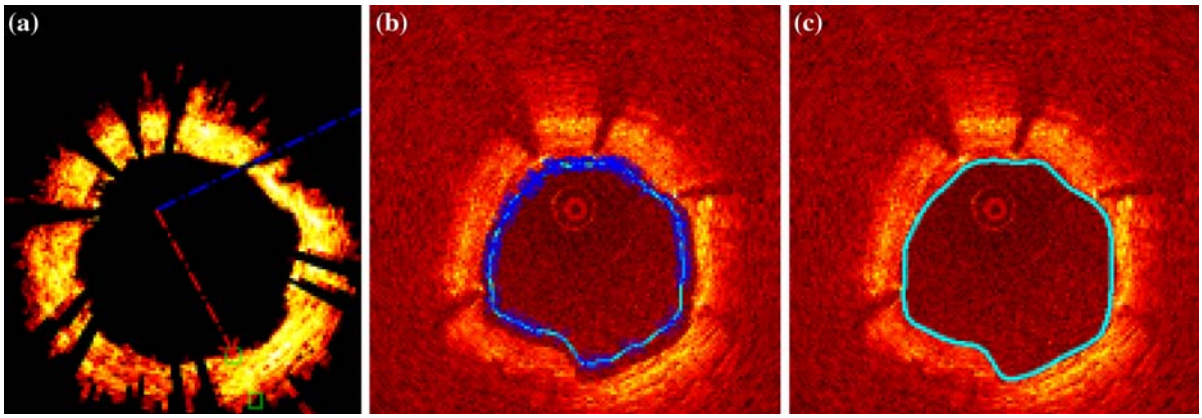

Fig. 3 **a** Ray shooting in prefiltered image, **b** initial spline on ray intersection points, **c** spline evolution result and segmented lumen region

spline contour. A cubic hermite spline, also known as a Catmull-Rom spline, which has four polynomial blending functions and whose control points are exactly on the spline contour is utilized. The interaction and initialization of the Catmull-Rom spline are practically well-suited to our problem for correction of the lumen contour and stent splines, if necessary. In the expert mode of our test application, we store such corrections for further improvement of our technique.

Spline initialization and propagation

For detection of the ROI, i.e. the inner and outer boundaries of the observable bright band in the OCT image, we utilize two splines, and initialize the spline control points by shooting rays in the "denoised image" from the center of the image to every direction. Thus, two Catmull-Rom splines are constructed to separate strut and shadow zone of image. This ROI is analyzed after the lumen spline propagates with update equations we designed in an active contour framework. In applying this approach to our problem, to increase the quality and speed of the solution, we developed a new and problem specific method. In addition, the parameters are adaptively determined and fixed for the propagation of the spline. Finally, the spline moves towards the lumen border and stops in the desired region as exemplified in Fig. 3.[2]

Shadow and strut detection

One important observation is that the OCT cross-section images which contain stent struts, generally include shadows behind the struts. The two splines we created in the previous steps of the algorithm form an ROI in the form of a band which separates the region of the shadows and struts. Analyzing the angular intensity energy distribution in the ROI provides clues to the shadow angles. To build such an energy map, rays are shot on the "row smoothed image" and the intersection points of these rays and the splines are computed. Interpolation of these two intersection coordinates (Fig. 4) and summation of corresponding image intensity values define the energy on a ray. Energies over all the rays are used

[2] A preliminary version of the details of our segmentation method appeared in [13].

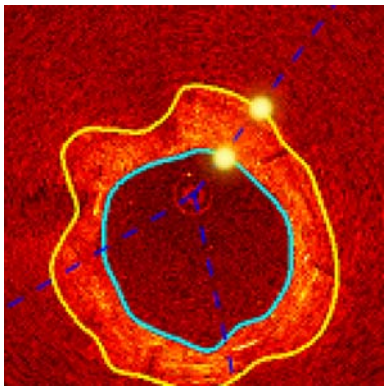

Fig. 4 Spline band over the ROI with beginning and end points for energy calculations

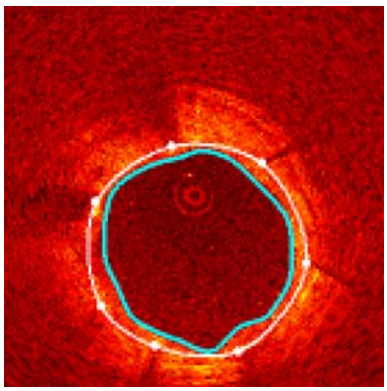

Fig. 5 Detected shadows and struts

for analyzing energy distribution characteristic of the overall image. Falling and rising of energy on these rays over some thresholds indicates the presence of strut shadows. A second analysis over the detected shadow rays is carried out between the two splines to detect the exact strut positions. A strut on a shadow ray is the maximum bright intensity pixel group and mostly negative deep gradient vectors follow such a group (Fig. 5). A linear search process in the band gives the strut positions. Our system makes this search operation in the original OCT image within the detected ROI.

For different NIH scenarios, we designed two modes of our system: (1) the new stent implants and minimum NIH cases; (2) mild to severe NIH cases. The shadow and strut detection differs with respect to the interpolation of the angular energy calculation: either starts from first spline to the middle range of the ROI, or from the middle of the ROI towards the

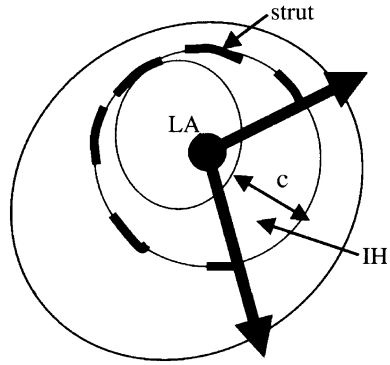

Fig. 6 Schematic of struts and related measurements calculated for stent follow-up analysis, adapted from [10]. We measured the maximum interstrut angle, LA (lumen cross-sectional area: L-CSA), IH (=Stent CSA − L-CSA), the various distances between the lumen and the stent contours, here c is depicted: the maximum distance = thickness of the NIH

outer field, respectively. Thus the range search varies and the strut detection thresholds are different but fixed for both modes.

Data analysis and statistics

Calibration

An important step is the z-offset calibration of the OCT pullback images based on the visualization of the imaging wire: images are obtained using a single-mode fibre-optic core that rotates within a transparent sheath with a known dimension of 0.0019". The image of the sheath appears as a small circle in middle of the display image and as a line in the rectangular image format. In our test application, the system calculates corresponding metric amount of a constant radius circle after adjusting the number of lines before the catheter line. The radius of this circle is set to 0.2 mm at the end of the calibration process.

Figure 6 depicts a diagram for the measurements carried out in our experiments for the strut assessment. Number of detected struts are counted, and the maximum angle between adjacent struts is measured. The lumen cross-sectional area (L-CSA) is calculated in mm^2 using the area of the lumen contour and the stent cross-sectional area (S-CSA) is calculated using the area of the stent contour. IH in Fig. 6 depicts the Intimal Hyperplasia area, defined as the area difference between the S-CSA and the L-CSA. We also compute the minimum, average and the maximum

distance (denoted by c in the figure) between the stent and the lumen boundaries in mm's.

Assessment of strut distribution

Manual strut detection is carried out by the expert in two ways: (1) using the LL system as the gold standard; (2) using our system with correction over the automatic results, abbreviated as the SF (Stent Follow-up) system. Our system allows the expert to make manipulations over the automatic detection result. The extracted lumen spline can be corrected, and the stent struts can be added, removed or marked. Automatic and corrected results are both displayed and stored to record the measurements for reporting.

The above two results (LL and SF) are compared with the automatic detection (ASF: Automatic Stent Follow-up) over a set of cross-section images from the OCT pullbacks in the dataset. The expert experimented over a total of 39 images with varying degrees of NIH.

The percentage of correctly detected struts is calculated over each image as follows: we count the total number of detected struts in each cross-section image. The percentage of correctly detected struts is set to 1 − normalized error, where the normalized error is defined as the absolute difference between the number of struts marked by the physician and the number of struts detected by our algorithm, which is later normalized by the physician marked strut count.

Another parameter calculated is the maximum interstrut angle measured from the center of the stent contour. This is the maximum angle between adjacent stent struts. As reported by Takebayashi et al. [10], this measurement correlates with the NIH thickness in IVUS-based studies.

NIH thickness was evaluated looking at the minimum, maximum, and the average distance between the lumen boundary and the stent. These parameters are calculated using the lumen border center and finding the distance between the lumen and the stent contours on rays extending from the lumen center.

Finally, stent eccentricity was calculated as the minimum divided by the maximum stent diameter.

Examples are shown in Fig. 7 for strut detection, lumen and stent boundary reconstruction in three different scenarios: (a) virtually no NIH; (b) minimum amount of NIH; (c) moderate NIH.

Results and discussions

Measurements of the lumen and the stent cross-sectional areas, and the number of stent struts are presented in Table 1 as given by the mean ± standard deviation (SD) values. This table shows comparisons between the automatic detection (ASF), the expert's adjustment of the automatic results (SF), and the expert's manual measurements using the LightLab software (LL). Bland-Altmann analysis revealed a mean difference for lumen cross-section area of 0.11 ± 0.70 mm^2 and for the stent cross-section area of 0.10 ± 1.28 mm^2.

The maximum angle between the stent struts, the minimum, average, and maximum distances between

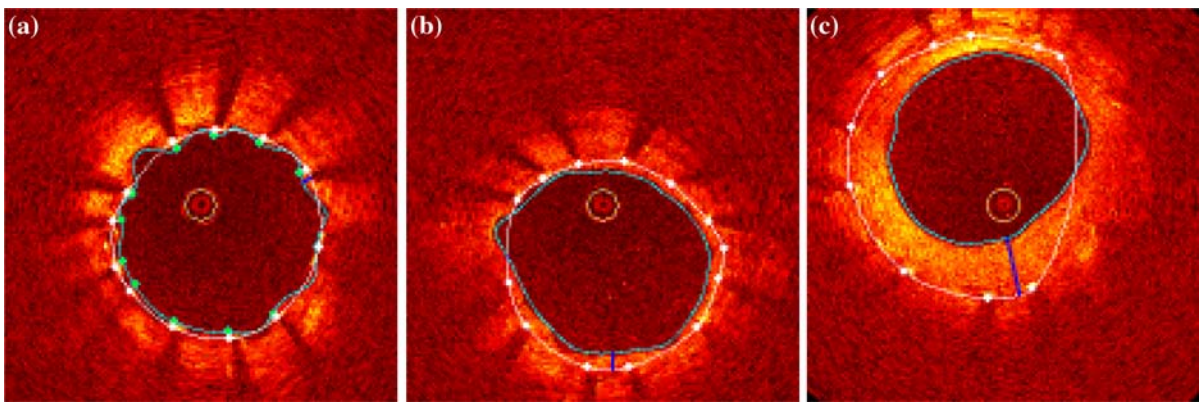

Fig. 7 Examples of strut detection, lumen and stent boundary reconstruction in three different scenarios: **a** NIH absent; **b** minimum amount of NIH; **c** moderate amount of NIH

Table 1 Strut assessment measurements compared among the expert manual detection with two different systems and the automatic detection

	Autodetection (ASF)	Expert manual adjustment (SF)	Expert manual measurement (LL)
Lumen CSA (mm^2)	5.78 ± 1.76	6.09 ± 1.85	6.05 ± 1.87
Stent CSA (mm^2)	6.59 ± 1.91	6.33 ± 1.66	6.26 ± 1.63
Stent struts, *n* normalized to (0,1)	0.91 ± 0.11	1.00 ± 0.00	1.00 ± 0.00

Values are mean ± SD

Table 2 Other strut assessment measurements compared between the expert manual detection and the automatic detection with our system

	Autodetection (ASF)	Expert manual adjustment/ measurement (SF)
Maximum angle between stent struts (°)	75.09 ± 26.63	85.96 ± 54.23
Maximum distance between stent and lumen border (mm)	0.31 ± 0.15	0.18 ± 0.13
Average distance between stent and lumen border (mm)	0.14 ± 0.07	0.08 ± 0.06
Minimum distance between stent and lumen border (mm)	0.02 ± 0.04	0.01 ± 0.02
Stent eccentricity	0.75 ± 0.11	0.80 ± 0.08

Values are mean ± SD

the stent and the lumen borders, and the stent eccentricity measurements are presented in Table 2 as given by the mean ± SD values. These measurements were not available from the LightLab software, hence, we report comparison between the autodetection and the manually adjusted results by the expert with our system.

In these first set of validation studies, our algorithm achieved a reasonably good accuracy in strut detection, which is around 91% ± 11%. The correlation (r^2 and *P* values) between the computer methods and the expert evaluations for lumen cross-section area was ($r^2 = 0.98$, P value < 0.0001), and for the stent cross-section area was ($r^2 = 0.85$, P value < 0.0001). For the detected number of struts the correlation was slightly lower: ($r^2 = 0.78$, P value < 0.0001). For our dataset: the lumen cross-sectional area was on the average (6.05 ± 1.87 mm^2), the stent cross-sectional area (6.26 ± 1.63 mm^2), the maximum inter-strut angle was on the average (85.96 ± 54.23°), the maximum, the average, and the minimum distance between the stent and the lumen were(0.18 ± 0.13 mm), (0.08 ± 0.06 mm), and (0.01 ± 0.02 mm), respectively, and stent eccentricity was (0.80 ± 0.08).

Limitations

In NIH scenarios, the shadow that corresponds to a stent strut is usually visible and detectable, however, there are situations where struts whose trailing shadows are not visible. Our work is ongoing for further improvements on such struts, which were missed with the shadow detection. The new generation of bio-degradable stents that do not demonstrate a bright strut and a shadow [14] cannot yet be detected by our approach.

Due to limitations of strut detection in NIH scenarios, the stent boundary reconstruction becomes more challenging and more prone to errors than that of the lumen. This difficulty caused a lower match between the automatic and manual computations based on the stent boundary such as the maximum distance calculation between the stent and the lumen border as observed in Table 2.

A further large-scale evaluation, which was beyond the scope of this initial manuscript describing a new algorithm for automated processing of OCT pullback and stent struts detection, will be necessary to correlate the degree of NIH and circumferential stent strut distribution, as suggested previously by IVUS [10].

Conclusions

We presented a new spline-based segmentation method for both the lumen boundary and stent strut boundaries, to assist in the problem of strut

distribution assessment. In addition, we proposed an energy map based automatic stent strut detection algorithm in OCT pullbacks. Our experimental results demonstrated that our algorithm works reasonably well on the segmentation of target boundaries in OCT images, and detected stent struts and their trailing shadows.

A strut distribution analysis was carried out and a number of measures important for stent implant follow-up and monitoring of the neointimal tissue growth over struts were calculated. Our system was compared against one expert evaluation and a 3rd party software requiring manual tracing and providing a limited number of derived parameters.

The conclusion from our study is that our new methods appear to offer a robust and reliable automated analysis of OCT pullbacks of coronary stented segments that might assist physicians in evaluating in-stent restenosis after PCI and study the vascular response of new stents and eluted drugs.

We are grateful to the entire staff of the catheterization laboratory of Columbia University (director Dr J Moses) in New York, USA, where the OCT recordings were performed.

References

1. Barlis P, Schmitt J (2008) Current and future developments in intracoronary optical coherence tomography imaging. EuroIntervention 4:529–534
2. Jang I, Bouma B, Kang D, Park S, Park S, Seung K, Choi K, Shishkov M, Schlendorf K, Pomerantsev E, Houser S, Aretz H, Tearney G (2002) Visualization of coronary atherosclerotic plaques in patients using optical coherence tomography: comparison with intravascular ultrasound. Am J Cardiol 39:604–609
3. Patwari P, Weissman NJ, Boppart SA, Jesser C, Stamper D, Fujimoto JG, Brezinski ME (2000) Assessment of coronary plaque with optical coherence tomography and high-frequency ultrasound. Am J Cardiol 85:641–644
4. Yabushita H, Bouma B, Houser S, Aretz H, Jang IK, Schlendorf K, Kauffman C, Shishkov M, Kang DH, Halpern E, Tearney G (2002) Characterization of human atherosclerosis by optical coherence tomography. Circulation 106:1640–1645
5. Xu C, Schmitt J, Carlier SG, Virmani R (2008) Characterization of atherosclerosis plaques by measuring both backscattering and attenuation coefficients in optical coherence tomography. J Biomed Opt 13(3):034003
6. Rieber J, Meissner O, Babaryka G, Oswald SRM, Koenig A, Schiele, T, Shapiro M, Theisen K, Reiser M, Klauss V, Hoffmann U (2006) Diagnostic accuracy of optical coherence tomography and intravascular ultrasound for the detection and characterization of atherosclerotic plaque composition in ex-vivo coronary specimens: a comparison with histology. Coron Artery Dis 17(5):425–430
7. Oh W, Yun S, Vakoc B, Shishkov M, Desjardins A, Park B, de Boer J, Tearney G, Bouma B (2008) High-speed polarization sensitive optical frequency domain imaging with frequency multiplexing. Opt Express 16(2):1096–1103
8. Lemos P, Saia F, Ligthart J, Arampatzis C, Sianos G, Tanabe K, Hoye A, Degertekin M, Daemen J, McFadden E, Hofma S, Smits P, de Feyter P, van der Giessen W, van Domburg R, Serruys P (2003) Coronary restenosis after sirolimus-eluting stent implantation: morphological description and mechanistic analysis from a consecutive series of cases. Circulation 108:257–260
9. Hwang CW, Wu D, Edelman ER (2001) Physiological transport forces govern drug distribution for stent-based delivery. Circulation 104:600–605
10. Takebayashi H, Mintz G, Carlier S, Kobayashi Y, Fujii K, Yasuda T, Costa R, Moussa I, Dangas G, Mehran R, Lansky A, Kreps E, Collins M, Colombo A, Stone G, Leon M, Moses J (2004) Nonuniform strut distribution correlates with more neointimal hyperplasia after sirolimus-eluting stent implantation. Circulation 110:3430–3434
11. Matsumoto D, Shite J, Shinke T, Otake H, Tanino Y, Ogasawara D, Sawada T, Paredes O, Hirata K, Yokoyama M (2007) Neointimal coverage of sirolimus-eluting stents at 6-month follow-up: evaluated by optical coherence tomography. Eur Heart J 28:961–967
12. Cook S, Ladich E, Nakazawa G, Eshtehardi P, Neidhart M, Vogel R, Togni M, Wenaweser P, Billinger M, Seiler C, Gay S, Meier B, Pichler W, Jni P, Virmani R, Windecker S (2009) Correlation of intravascular ultrasound findings with histopathological analysis of thrombus aspirates in patients with very late drug-eluting stent thrombosis. Circulation (Epub 2009 Jul 20) 120(5):391–399
13. Gurmeric S, Unal G, Carlier S, Yang Y, Slabaugh G (2008) Automatic stent implant follow-up in intravascular optical coherence tomography images. In: MICCAI-CVII: the international workshop on computer vision for intravascular imaging
14. Ormiston J, Serruys P, Regar E, Dudek D, Thuesen L, Webster M, Onuma Y, Garcia-Garcia H, McGreevy R, Veldhof S (2008) A bioabsorbable everolimus-eluting coronary stent system for patients with single de-novo coronary artery lesions (absorb): a prospective open-label trial. Lancet 371(9616):899–907